Multiple-Sensor Weigh-in-Motion: Theory and Experiments

D. CEBON AND C. B. WINKLER

A theory is developed for the design of multiple-sensor weigh-in-motion (WIM) systems to minimize the errors caused by the dynamic axle loads of heavy vehicles moving at highway speeds. The theory is verified using measurements from a wheel load measuring mat of total length 38 m, incorporating 96 capacitive strip WIM sensors. The mat was installed on the Navistar test track in Indiana. A total of 460 test runs was performed on six different articulated heavy vehicles, at a range of speeds between 8 and 80 km/hr. The strip sensors were found to be reliable and to measure the dynamic wheel loads with errors of less than 4 percent RMS. The sensor calibration is independent of speed and temperature. The experimental results were found to agree closely with the theoretical predictions of multiple-sensor WIM performance and it was possible, using a three-sensor array, to measure static axle loads with approximately 6 percent RMS error, or less, for typical highway conditions of speed and road surface roughness. A good design for multiple-sensor WIM systems is to use three sensors, spaced evenly along the road. The sensors should be spaced according to a simple formula that depends only on the average traffic speed and the number of sensors.

A single weigh-in-motion (WIM) sensor measures the instantaneous dynamic force generated by each measured axle. This force can be significantly different to the static axle load that would be measured on a conventional static vehicle scale. One of the main reasons for the difference is the dynamic variation of the tire force caused by vibration of the vehicle as it is excited by road surface roughness. These dynamic axle loads typically have RMS amplitudes of 10 to 30 percent of the static axle loads of heavy goods vehicles (*1–4*). Thus the accuracy of a WIM system with one sensor is limited fundamentally by the dynamics of the vehicles being measured, and typical RMS errors of existing single-sensor systems are 12 to 29 percent (*5*).

The advent of low-cost WIM sensors provides the possibility of using two or more sensors along the road to compensate for the effects of dynamic forces in the determination of static axle loads. The main objective of the work described here is to investigate, theoretically and experimentally, the design and performance of multiple-sensor WIM arrays that are intended to measure the static axle loads of vehicles traveling at highway speeds.

THEORY OF MULTIPLE-SENSOR WEIGH-IN-MOTION

The outputs of several sensors in a WIM array might be processed in a variety of different ways to yield an estimate of the static loads. Some possibilities are described by Glover (*6*), who performed numerical simulations of the outputs of WIM arrays with 1, 2, 9, 19, and 81 sensors with a variety of spacing arrangements, including uniform, linear, geometric, and logarithmic. Glover achieved good results for a nine-sensor, evenly spaced array, using a least squares procedure to correct the simulated forces for the dominant Fourier component.

Evenly spaced WIM arrays are examined. It is assumed that the outputs of the individual sensors are averaged to yield an estimate of the static loads. The simple averaging method requires few sensors and little computation to give comparable accuracy to more sophisticated curve fitting methods (*5,6*).

Sinusoidal Input

It is useful to begin the analysis by calculating the output of a multiple-sensor WIM array to a sinusoidal force $p(t)$ defined by

$$p(t) = P_0 + P \sin(\omega t + \phi) \tag{1}$$

where

P_0 = static tire force,
P = dynamic tire force amplitude,
ω = angular frequency,
ϕ = arbitrary phase angle, and
t = time.

The force is considered to move at constant speed V over an array of n sensors that are evenly spaced a distance Δ apart, as shown in Figure 1. The sensors are assumed to be noiseless and perfectly accurate so that the output of each sensor is the instantaneous dynamic load applied to the sensor by $p(t)$. The output of the array, taken to be the arithmetic mean of the individual sensor outputs, is denoted $\bar{P}$. It was found by Glover (*7*) that the peak array output error $\hat{\varepsilon}$, which occurs for the worst-case value of ϕ, is given by

$$\hat{\varepsilon}(n, \delta) = \pm\{2\,\mathrm{E}[\varepsilon(n, \delta, \phi)]^2\}^{1/2} = \pm\left[\frac{1}{n} + \frac{2}{n^2}\sum_{k=1}^{n}(n - k)\cos(k2\pi\delta)\right]^{1/2} \tag{2}$$

where

E[ ] = expectation operator;
k = dummy integer variable;
ε = nondimensional WIM error, defined by

D. Cebon, Engineering Department, Cambridge University, Trumpington Street, Cambridge, CB2 1PZ, England. C. B. Winkler, University of Michigan Transportation Research Institute, 2901 Baxter Road, Ann Arbor, Mich. 48109.

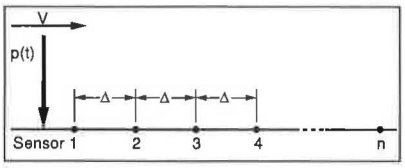

FIGURE 1 Cross section of an *n*-sensor WIM array, traversed by force *p(t)* at speed *V*.

$$\varepsilon(n, \delta, \phi) = (\bar{P} - P_0) \tag{3}$$

δ = nondimensional sensor spacing, defined by

$$\delta = \omega\Delta/2\pi V = \Delta/(V/f). \tag{4}$$

Figures 2a–d show $\hat{\varepsilon}(n, \delta)$ for $n = 2$ to 5. Three observations are made:

1. The error $\hat{\varepsilon}$ is unity for integer values of δ, which correspond to the sample points (sensors) being spaced an integer number of dynamic force cycles apart.
2. On each graph in Figure 2, there are $(n - 1)$ zeros at values of $\delta = \delta_k$ corresponding to

$$\delta_k = k/n, \qquad k = 1, 2, 3, \ldots, (n - 1) \tag{5}$$

Thus the range of δ between the first and last zeros on each graph increases with n: $\delta_1 = 1/n$ to $\delta_{n-1} = (n - 1)/n$. This is the region in which $\hat{\varepsilon}$ is consistently small.

3. The curves for $0 \leq \delta < 1$ repeat for each integer value of δ and are symmetric about $\delta = 0.5, 1.5, 2.5$, etc. This can be verified by plotting Equation 2 for $\delta > 1$ (*7*). The repetition is a form of aliasing with a Nyquist spacing of $\delta = 0.5$. There is no apparent benefit in using $\delta > 1$ in a WIM array.

Stochastic Input

For particular values of n, V, and Δ, Equation 2 can be considered to be the transfer function of a linear filter that yields the worst-case error for dynamic force components of frequency ω. Using the standard input-output relationship for a linear system subject to ergodic random excitation (*8*), the mean square direct spectral density of the measurement error $S_{ee}(\omega)$ because of the two-sided input tire force spectral density $S_{pp}(\omega)$ is given by

$$S_{ee}(\omega) = \hat{\varepsilon}(n, \omega\Delta/2\pi V)^2 \, S_{pp}(\omega) \qquad -\infty < \omega < \infty. \tag{6}$$

For a linearized vehicle model, $S_{pp}(\omega)$ can be found from the road profile input displacement spectral matrix $[\mathbf{S}_u(\omega)]$ and a vehicle transfer function matrix $[\mathbf{H}(\omega)]$, as described by Newland (*8*) and Robson (*9*). Equation 6 can then be integrated with respect to frequency and used to obtain the RMS array error $\sigma(n)$ for an n-sensor system, traversed by a linearized vehicle model:

$$\sigma(n) = \left\{ 2\int_0^\infty \hat{\varepsilon}(n, \omega\Delta/2\pi V)^2 [\mathbf{H}(\omega)]^* [\mathbf{S}_u(\omega)] [\mathbf{H}(\omega)]^T d\omega \right\}^{1/2} \tag{7}$$

where the asterisk (*) denotes the complex conjugate and T denotes the matrix transpose. $[\mathbf{H}(\omega)]$ can be determined easily from the equations of motion of a vehicle model (*8*).

Equation 7 yields the RMS error for one random tire force that is statistically stationary and is passing over an ensemble of n-sensor WIM arrays. It can also be considered to be the expected standard deviation of the static load estimation error for many different axles, with similar dynamic characteristics, passing over a single WIM site. This assumes that the wheel forces are sampled from an ergodic random process, which is reasonable under most circumstances (*9*). It also assumes that the surface of the WIM array is not abnormally rough and that the individual suspensions all generate similar tire force spectral densities.

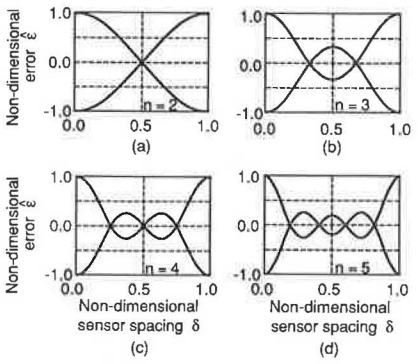

FIGURE 2 Plots of the envelope error $\hat{\varepsilon}$ from Equation 2: (a) $n = 2$, (b) $n = 3$, (c) $n = 4$, and (d) $n = 5$.

Measures of WIM System Performance

It is useful to define some nondimensional measures of WIM system performance. The error coefficient of variation (ECOV) $\rho(n)$, for an n-sensor system is defined by

$$\rho(n) = \sigma(n)/P_0 \tag{8}$$

where P_0 is the static axle load.

It is easily shown that the ECOV for a single-sensor array, $\rho(1)$, is equal to the dynamic load coefficient (DLC), which is the ratio of the RMS dynamic load to the static load (*7*). For highway conditions of road roughness and speed, DLC values in the range 0.1 to 0.3 are typical (i.e., 10 to 30 percent RMS single-sensor WIM error), but DLC values up to 0.4 have been measured for particularly poorly damped tandem suspensions (*1,4*).

The proportional improvement in the estimate of static load measurement accuracy relative to a single-sensor WIM system is denoted here as the static accuracy coefficient (SAC), $\eta(n)$, which is defined by

$$\eta(n) = \frac{\rho(1) - \rho(n)}{\rho(1)} = \frac{\text{DLC} - \rho(n)}{\text{DLC}} \tag{9}$$

A single-sensor WIM system will yield $\rho(1) = \text{DLC}$ and $\eta(1) = 0$, whereas perfect WIM system performance corresponds to $\rho(n) = 0$, and hence $\eta(n) = 1$.

Simulation Models

Vehicle Model

Experimental and theoretical studies (*1–3,10*) have shown that low-frequency (1.5- to 4.5-Hz) sprung mass modes of vehicle bounce and pitch vibration usually dominate the dynamic tire forces generated by heavy vehicles on highways. The main exception occurs for vehicles with axle group suspensions (particularly of the walking-beam type) with poorly damped bogie pitching modes that can generate large dynamic forces in the 8- to 15-Hz frequency range. However, these suspensions are only found on a small proportion of heavy goods vehicles: approximately 15 percent of new tractors, and less than 2 percent of trailers in the United States (*11*).

The simple generic ¼-car vehicle model shown in Figure 3 was chosen for this study to represent the majority of truck suspensions that generate a large low-frequency wheel force spectral peak caused by sprung mass motion. It has a sprung mass natural frequency of approximately 1.9 Hz. Results are also presented by Cebon and Winkler (*7*) for a model that represents those suspensions (in the minority), which generate large dynamic wheel loads caused by unsprung mass motion.

The generic vehicle model does not contain the detailed suspension nonlinearities and complexities of sprung mass motion that are typical of heavy vehicles (*10*); however, the wheel force spectral densities are sufficiently representative for the purpose of this study of WIM systems.

Derivation of the equations of motion and formation of the transfer function matrix $[\mathbf{H}(\omega)]$ and input spectral matrix $[\mathbf{S}_u(\omega)]$ are straightforward and will not be discussed here (*7*).

Road Surface Profile Spectral Density

The road profile displacement spectral density $\mathbf{S}_u(\gamma)$, at wavenumber γ, used to generate $[\mathbf{S}_u(\omega)]$ in the simulation study was a two-index function recommended elsewhere (*12*):

$$\mathbf{S}_u(\gamma) = \begin{cases} \mathbf{S}(\gamma_0)|\gamma/\gamma_0|^{-n_1} & |\gamma| \le \gamma_0 \\ \mathbf{S}(\gamma_0)|\gamma/\gamma_0|^{-n_2} & |\gamma| > \gamma_0 \end{cases} \quad (10)$$

The values used for the various constants were $n_1 = 2.0$, $n_2 = 1.5$, $\gamma_1 = 1.0$ rad/m and $\mathbf{S}(\gamma_0) = 1.275 \times 10^{-6}$ m³/rad, which corresponds to the good road surface classification (*12*). This profile may be likened to a good U.S. highway surface.

Simulation Results

Figure 4 shows the wheel force spectral density $S_{pp}(\omega)$ and the error spectral density $S_{ee}(\omega)$ (as calculated by Equation 6) for the vehicle model traveling at 100 km/hr over a three-sensor WIM array with a sensor spacing of $\Delta = 4$ m. The same data are plotted on both linear and logarithmic scales. On the linear graph, the area under the solid line is proportional to DLC² and the area under the dashed lines is proportional to $\rho(3)^2$. The logarithmic graph is provided to show more clearly the attenuation of $S_{pp}(\omega)$ caused by $\hat{\varepsilon}(n, \omega\Delta/2\pi V)^2$. Because the maximum value of $\hat{\varepsilon}(n, \delta)$ is unity, (Figure 2), $S_{ee}(\omega)$ can never exceed $S_{pp}(\omega)$, hence the dashed line can never cross the solid line. This means that for perfectly accurate sensors, $\rho(n)$ can never exceed the DLC value.

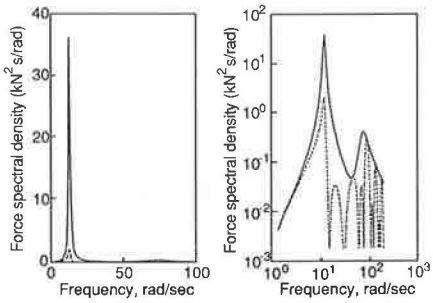

FIGURE 4 Tire force spectral density $S_{pp}(\omega)$ and WIM array error spectral density $S_{ee}(\omega)$ for the vehicle model traveling at 100 km/hr over a WIM array with $n = 3$ and $\Delta = 4$ m. Solid line = $S_{pp}(\omega)$; broken line = $S_{ee}(\omega)$.

Performance data corresponding to this simulation were DLC = 0.142, $\rho = 0.051$ and $\eta = 0.645$. Thus in this case, the three-sensor array reduces the error coefficient of variation from 14.2 to 5.1 percent, which corresponds to a 64.5 percent improvement in performance over a single-sensor WIM system. This averaging scheme clearly improves substantially the accuracy of static wheel load prediction.

Figures 5a and b show the influence of the sensor spacing Δ on the ECOV ρ and the SAC η, for $n = 3$, with the vehicle model traveling at speeds of 60 and 100 km/hr. It is apparent

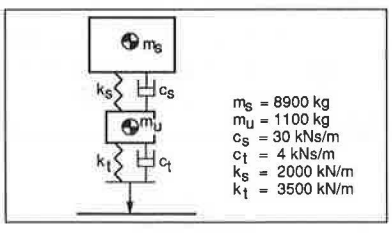

FIGURE 3 Schematic diagram of the two degrees of freedom, quarter-car vehicle model.

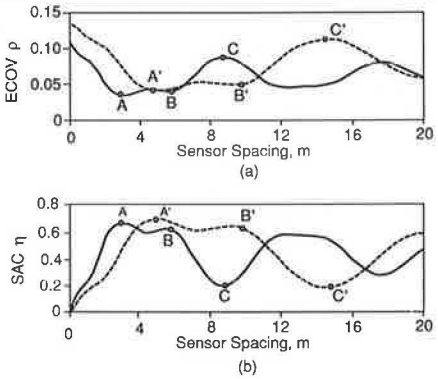

FIGURE 5 Variation of theoretical WIM system performance with sensor spacing Δ. Points A, B, C, etc., were calculated according to the theory for sinusoidal inputs. Solid line = 60 km/hr; broken line = 100 km/hr. (a) error coefficient of variation ρ, and (b) static accuracy coefficient η.

that for each speed there is a range of spacings for which the WIM ECOV is low, i.e., the system performs relatively accurately.

The shape of the ECOV curves is closely related to the magnitude of the error envelope curve $|\hat{\varepsilon}(n = 3, \delta)|$ shown in Figure 2b; however, because the system is subjected to an approximately narrow-band random input (centered on the sprung mass natural frequency of the vehicle) instead of a single sine wave, the ECOV curve is a smoothed version of $|\hat{\varepsilon}|$.

The properties of the $\hat{\varepsilon}$ curves described earlier can be used to understand the features of the ECOV curves. From Equation 5, the first two zeros in $\hat{\varepsilon}(3, \delta)$ occur when $\delta_k = \delta_1 = \frac{1}{3}$ and $\delta_2 = \frac{2}{3}$. These points are expected to correspond approximately to minima in the ECOV curves. Using the definition of δ from Equation 4, with $V = 16.7$ m/sec (60 km/hr) and $f = \omega/2\pi = 1.9$ Hz [the dominant resonant frequency in $S_{pp}(\omega)$], the minima are expected to occur approximately at $\Delta = V/3f = 2.9$ m and $\Delta = 2V/3f = 5.9$ m. These points are labeled A and B on Figure 5. The corresponding points for $V = 27.8$ m/sec (100 km/hr) are labeled A' and B'. Conversely, the worst errors are expected to occur when $|\hat{\varepsilon}(3, \delta)| = 1$. This happens when the dominant (resonant) frequency component in $S_{pp}(\omega)$ is sampled once every cycle (or once every two cycles), i.e., for integer values of δ. The points labeled C and C' on Figure 5 correspond to $\delta_3 = 1$. The labeled points on Figure 5 are all slightly to the right of the maxima and minima of the ECOV curves at which they might be expected to occur because $S_{pp}(\omega)$ is not symmetric about the main spectral peak (Figure 4).

WIM Array Design

The WIM array is designed to be accurate for the widest possible range of vehicles (frequencies) and speeds. For given values of Δ and f, it is possible to estimate the range of vehicle speeds V over which the system will operate in the plateau region of the ECOV curve, where the accuracy is consistently high ($\eta \geq 0.5$).

From Equation 5, the zeros in $\hat{\varepsilon}(n, \delta)$ occur when $\delta_k = k/n$, $k = 1, 2, 3, \ldots, (n - 1)$. We will ignore values of $k > n$, because these represent large (often impractical) sensor spacings at which the wheel forces are sampled at frequencies well below the Nyquist frequency: i.e., less than two sample points per cycle. Using Equations 4 and 5, and assuming fixed Δ and f, the zeros occur at speeds V_k given by

$$V_k = \frac{\bar{f}n\Delta}{k} \text{ (m/sec)}, \qquad k = 1, 2, 3, \ldots, (n - 1) \tag{11}$$

and $\bar{f}$ is the frequency in Hz of the dominant spectral component in $S_{pp}(\omega)$.

The plateau region of the ECOV curve will be governed by the first and last zeros in $\hat{\varepsilon}$: $k = 1$ and $k = n - 1$. Thus the maximum and minimum speeds for which the WIM system will be reasonably accurate (operating in the plateau region) are given by

$$V_{max} = V_1 = \bar{f}n\Delta$$

and

$$V_{min} = V_{n-1} = \bar{f}n\Delta/(n - 1) \qquad \text{(m/sec)}, \qquad n > 1 \tag{12}$$

A good design procedure would be to select Δ such that the average traffic speed $\bar{V}$, in m/sec, corresponds to the average of V_{min} and V_{max}. Thus, from Equation 12:

$$\Delta_{design} = \frac{2(n - 1)\,\bar{V}}{\bar{f}n^2} \qquad n > 1 \tag{13}$$

There is considerable variation in the dominant frequencies $\bar{f}$ in the dynamic wheel force spectra of common heavy vehicles. They are usually in the range 1.5 to 4.5 Hz and a suitable average value is $\bar{f} = 2.5$ Hz. It is possible that a slightly higher average frequency (say $\bar{f} = 3.0$ Hz) may be more suitable for WIM systems in countries where heavy-vehicle suspensions are relatively stiffer.

Figure 6 shows a design chart for multiple-sensor WIM arrays using Equation 13 with $\bar{f} = 2.5$ Hz and speeds of 20, 40, 60, 80, and 100 km/hr. It yields values of Δ_{design} for arrays with $n = 2$ to 10 sensors.

Sensitivity to Frequency and Speed

Substituting the design spacing Δ_{design} from Equation 13 into Equation 12 gives

$$V_{max} = 2(n - 1)\bar{V}/n \tag{14a}$$

and

$$V_{min} = 2\,\bar{V}/n \qquad n > 1 \tag{14b}$$

If $n = 2$, $V_{min} = V_{max} = \bar{V}$. Thus a two-sensor WIM system can only be designed to be accurate at one speed. If $n = 3$, however, $V_{min} = \frac{2}{3}\bar{V}$ and $V_{max} = \frac{4}{3}\bar{V}$ and a system with sensor spacing chosen according to Equation 13 will be accurate for speeds of $\frac{2}{3}\bar{V} \leq V \leq \frac{4}{3}\bar{V}$. For example if $\bar{V} = 80$ km/hr, this would yield $53 \leq V \leq 107$ km/hr. Similarly, if $n = 4$, the range of accurate performance is given by $\frac{1}{2}\bar{V} \leq V \leq \frac{3}{2}\bar{V}$.

Figures 7a and b show the ECOV (ρ) and SAC (η), respectively, for two-, three-, and four-sensor WIM systems when traversed by the vehicle model. The arrays were designed for an average speed of 80 km/hr ($\bar{V} = 22.2$ m/sec) according to Equation 13 with $\bar{f} = 1.9$ Hz. Also shown in

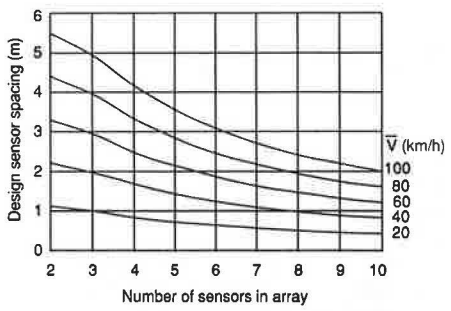

FIGURE 6 Design chart for multiple-sensor WIM systems using Equation 13 with $\bar{f} = 2.5$ Hz.

Figure 7a is ρ(1) (DLC) for comparison. The following observations are made:

1. The WIM array with only two sensors provides a significant improvement in accuracy over the single-sensor system (DLC), in the vicinity of the design speed of 80 km/hr.
2. The two-sensor system loses accuracy quickly for speeds away from 80 km/hr, whereas the three-sensor system has an accurate plateau region for $53 \leq V \leq 107$ km/hr, as expected. The four-sensor system is accurate over an even wider speed range.
3. In the vicinity of 80 km/hr, an increase in the number of sensors yields only a modest increase in accuracy ($\eta = 0.6$ for $n = 2$, $\eta = 0.67$ for $n = 4$).
4. For speeds less than about 30 km/hr, the ECOV (ρ) and SAC (η) curves fluctuate rapidly because of aliasing.

From Figure 7, it appears that three sensors is a good choice, because the system is reasonably accurate and has a relatively wide operating speed range. The four-sensor system yields a larger speed range with only a small accuracy improvement over the three-sensor system. The extra cost of the fourth sensor may not be worthwhile in practice.

The range of frequencies over which the WIM array will be accurate for a given vehicle speed $\bar{V}$ can be found using Equations 4 and 5 and replacing Δ by Δ_{design} from Equation 13:

$$f_{min} = n\bar{f}/2(n - 1) \tag{15a}$$

and

$$f_{max} = n\bar{f}/2, \qquad n > 1 \tag{15b}$$

Thus, if $n = 2$, $f_{min} = f_{max} = \bar{f}$, that is, the system can only be tuned to perform well at one input frequency. If $n = 3$, the operating frequency range (for a fixed speed) is approximately $\frac{2}{3}\bar{f} \leq f \leq 2\bar{f}$. For $\bar{f} = 2.5$ Hz this gives $1.9 \leq f \leq 3.8$ Hz. Similarly, if $n = 4$, the operating frequency range is $\frac{2}{3}\bar{f} \leq f \leq 2\bar{f}$, which, for $\bar{f} = 2.5$ Hz, yields $1.7 \leq f \leq 5$ Hz. Thus, $n = 3$ is a reasonable choice, although errors may occur when the frequency and speed take extreme values simultaneously. The worst error is likely to occur when $V \approx V_{min}$ and $f \approx f_{min}$, although the other extreme condition ($V \approx V_{min}$ and $f \approx f_{max}$) may also yield significant errors.

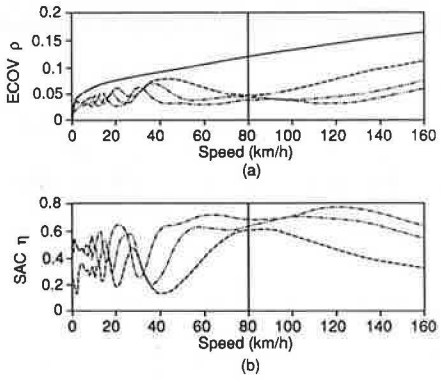

FIGURE 7 Influence of speed on the theoretical performance of two-, three-, and four-sensor WIM systems, designed for an average traffic speed of 80 km/hr. Solid line, $n = 1$ (DLC); dashed line, $n = 2$; double dotted line, $n = 3$; and single dotted line, $n = 4$. (a) error coefficient of variation ρ, and (b) static accuracy coefficient η.

EXPERIMENTAL PROGRAM

Wheel Load Measuring Mat

The load measuring mat used in this project was developed by Cole and Cebon (*13*) at Cambridge University in the United Kingdom, in conjunction with Golden River UK Ltd. It incorporated novel WIMstrip capacitive strip sensors that are inexpensive, reliable, and potentially more accurate than other existing low-cost WIM sensors. The sensors had approximate cross section of 9 × 30 mm and length 1.2 m. They were encapsulated in stiff polyurethane tiles of dimensions 1.2 × 1.2 × 13 mm thick, with three sensors per tile, laid transverse to the wheel path at a spacing of 400 mm between sensors. Thirty-two tiles, containing a total of 96 sensors, were obtained for the project. The tiles were mounted end-to-end on the test track, to provide an instrumented test section of length 38.4 m along one wheel track.

A schematic cross section of an encapsulated WIMstrip sensor is shown in Figure 8. Tire contact pressure applied to the top surface of the mat causes the top plate of the aluminum extrusion to deflect and hence the air gap between the top plate and the inner copper electrode is reduced. This results in an increase in the capacitance of the device, which, with appropriate processing, can be related directly to the contact pressure change. In order to determine the instantaneous wheel load, it is necessary to integrate the transducer output with respect to time for the duration of the tire contact. Details of the sensor design and some sources of error are discussed by Cole and Cebon (*13*).

The mat installation used six Golden River Marksman 600 data loggers. Each sensor was attached to a data logger by a 5-m-long cable and each data logger processed the outputs of 16 sensors, performed the integration described, and stored the results. The data loggers were connected into a network in a daisy-chain configuration by RS232 serial data cables. An IBM PC-AT microcomputer was connected to the network and used to upload the raw axle load information from the data loggers after each vehicle test run. (A load-measuring mat of practically any length can be constructed simply by adding more tiles and data loggers.)

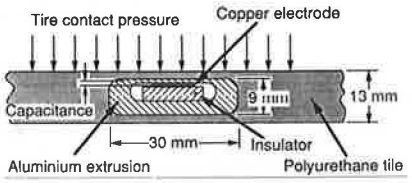

FIGURE 8 Schematic cross section of a capacitive strip wheel force sensor encapsulated in a polyurethane tile.

Test Site and Vehicles

The field tests were performed on the Navistar test track in Fort Wayne, Indiana. The oval track has two lanes and is 1.9 km long. The polyurethane mat tiles were attached to the test track with a sheet of double-sided adhesive tape and 12 masonry anchors per tile, screwed into the asphalt road surface. A timber sheet of total length 19.5 m, width 1.2 m, and thickness 13 mm was screwed to the test track at each end of the mat installation. This ensured that the vehicles were nominally horizontal when passing over the mat sensors, and that transient vibration caused by the 13-mm step was reduced slightly.

Three 6 × 4 tractors and three tandem-axle semitrailers were provided by Navistar for testing on the mat. The vehicles were arranged into six different tractor and semitrailer combinations (denoted S1 to S6). Two of the tractors had tandem four-spring suspensions and the third had a trailing-arm tandem air suspension with hydraulic dampers. Two of the trailers had four-spring tandem suspensions, whereas the third had a pivoted-spring single-point tandem suspension. The vehicle combinations were selected to be reasonably representative of the U.S. truck fleet. Each vehicle was weighed on a static vehicle scale immediately before or after the testing. The weighing procedure involved driving the vehicle onto and then off of the scale, one axle at a time, and recording the weight of each axle combination. This procedure enabled an estimate of the static load of each axle to be obtained as well as the gross weight of the vehicle. [Cebon and Winkler (*7*) provide detailed information about the vehicles and axle loads.]

Each articulated vehicle combination was driven over the mat at nominal speeds of 8, 16, 32, 48, 64, and 80 km/hr (5, 10, 20, 30, 40, 50 mph) in both directions. At least six repetitions were performed for each test condition, giving a total of 460 test runs during 4 days of testing. The surface temperature of the mat was measured before each vehicle test.

Sensor Performance

Detailed information concerning the performance of the sensors was provided by Cebon and Winkler (*7*). The important results are summarized here.

Calibration and Accuracy

Three methods were used to calibrate the sensors and test their uniformity. The first two used purpose-built hydraulic static calibrators (*13*). With this approach, the coefficient of variation of the calibration factors measured at three points along the length of each sensor was found to average 3.2 percent when measured on bare sensors and 4.5 percent when measured on the same sensors after being cast into the mats. (It is believed, but not rigorously demonstrated, that this difference is caused mostly by experimental difficulties in the second procedure, not to true performance differences.)

The third calibration was done at the test site by driving each of the six vehicles over the mats at 8 km/hr (5 mph) and comparing readings for the steer axles with the known values of their static loads. Careful analysis of these data (*7*) reveals that the average baseline sensor error (i.e., with respect to the true applied load) is less than 4 percent. The error can be attributed to noise and calibration errors.

Sensitivity to Temperature

No systematic dependence of sensor output on temperature was measurable for mat surface temperatures of 15°C to 40°C.

Sensitivity to Speed

No systematic dependence of static load errors on vehicle speed could be detected and no evidence could be found of fore-aft weight transfer affecting the static loads for higher speeds. It is concluded, therefore, that the response of the capacitive strip transducers is not affected significantly by vehicle speed.

Reliability

Approximately 2.5 percent of all data was lost out of 460 test runs over the 96 sensors. Almost half of the lost data (1 percent) was caused by a single sensor that failed. The remainder was caused by false triggers of the data loggers. (This problem has subsequently been rectified.)

Drift with Time

Insufficient time was available to detect any long-term drift in calibration. Glover and Newton (*5*) performed similar tests on an installation of WIMstrip sensors mounted in slots cut in the TRRL test track in England. They did not detect any significant drift in sensitivity during the 7-month testing period in 1989.

WIM PERFORMANCE FOR SIX ARTICULATED VEHICLES

The mat data files for the six articulated vehicles were processed to determine the ECOV (ρ) as a function of WIM array design parameters (n and Δ), for each axle of each vehicle at the six nominal testing speeds (8, 16, 32, 48, 64, 80 km/hr). Figure 9 shows an example of the procedure, in which many three-sensor WIM arrays ($n = 3$) with $\Delta = 1.6$ m can be obtained by averaging the outputs of appropriately spaced groups of sensors. Averages of this type were calculated for sensor spacings $\Delta = 0, 0.4, 0.8, \ldots, 12$ m, and $n = 2$ to 6 sensors, i.e., 155 different WIM array configurations in all.

Because of space limitations, only a limited number of experimental results are presented here. The remaining results are presented by Cebon and Winkler (*7*).

Histograms of WIM force averages are provided for vehicle S4 traveling at a speed of 85 km/hr in Figures 10a, b, and c. Figure 10a shows the force distribution for Axle 5 on the trailer, calculated by considering each transducer to be a separate WIM system (i.e., by setting $\Delta = 0$). Figure 10b shows

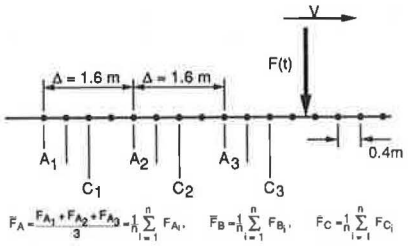

FIGURE 9 Showing the calculation of three-sensor WIM averages with a spacing of Δ = 4 × 0.4 = 1.6 m using data from the mat.

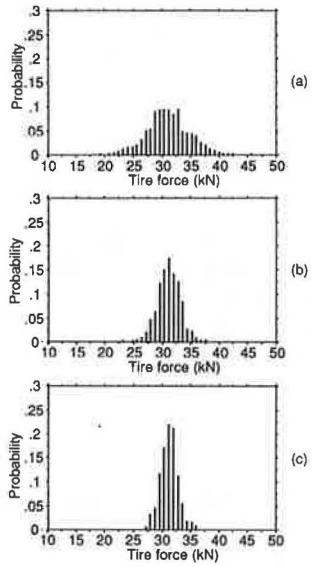

FIGURE 10 Histograms of WIM average force, Vehicle S4, Axle 5, speed = 85 km/hr: (a) single sensor; (b) three sensors, Δ = 4.0 m; and (c) six sensors, Δ = 2.4 m.

the result of analyzing the same data as Figure 10a, but with three-sensor arrays ($n = 3$) and $\Delta = 4.0$ m. (This array spacing was determined using equation 13 with $\overline{V}$ set to the testing speed (24 m/sec) and $\overline{f} = 2.5$ Hz.) Similarly, Figure 10c shows the result of analyzing the same data with six-sensor averages ($n = 6$) and $\Delta = 2.4$ m. It is apparent from the figures that the spread of the probability distribution (which is proportional to the ECOV) is reduced considerably by performing the three-sensor averages. The ECOV (ρ) is reduced from 11.5 percent for the single-sensor system to 5.7 percent for the three-sensor system and 4.2 percent for the six-sensor system.

Comparison of Experiment and Theory

A graph of ρ versus Δ for the steering axle of Vehicle S1 at 32 km/hr (9 m/sec) is provided in Figure 11a. The vertical

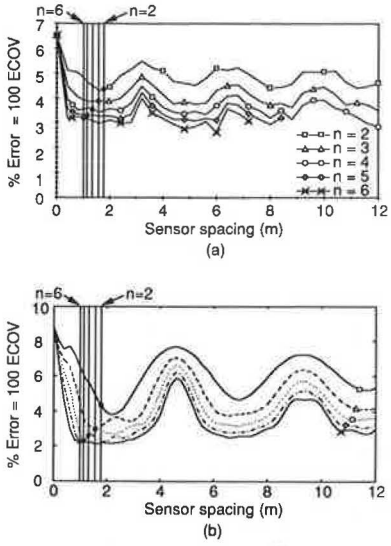

FIGURE 11 WIM array ECOV ρ versus sensor spacing Δ. Vertical lines indicate design spacings according to Equation 13 with $\overline{V}$ = 9 m/sec, $\overline{f}$ = 2.5 Hz. (a) Experimental results for Vehicle S1, steering axle, speed 32 km/hr; and (b) theoretical results for quarter-car model, speed = 32 km/hr.

lines on the figure labeled $n = 2$ to 6 correspond to the design spacing Δ_{design} as calculated from Equation 13 with $\overline{V} = 9$ m/sec and $\overline{f} = 2.5$ Hz. Figure 11b shows theoretical curves that were calculated using Equation 7 for the ¼-car vehicle model, traveling at 32 km/hr. The vertical lines on the figure again show the design spacings, calculated using Equation 13 with $\overline{V} = 9$ m/sec and $\overline{f} = 2.5$ Hz. Several comments can be made about Figures 11a and b.

The general shapes and magnitudes of the experimental and theoretical curves are similar. This appears to verify that the ¼-car model used in the theoretical analysis is a reasonable representation of the dynamics of the steering axle of Vehicle S1.

The main differences between the theoretical and experimental curves are the spacings at which the peaks and troughs occur. This is because the natural frequencies of the test vehicle and the theoretical model are different. The theoretical model had a sprung mass natural frequency of 1.9 Hz. The natural frequency of the experimental vehicle can be deduced from Figure 11a by considering the location of the first peak, which occurs approximately at $\Delta = 3.2$ m, corresponding to $\delta = 1$. Using Equation 4, the natural frequency of the vehicle is given by

$$f = V/\Delta_1 \tag{16}$$

where Δ_1 – sensor spacing corresponding to the first peak in the curve of ρ versus Δ. From Figure 11a, $\Delta_1 = 3.2$ m, and using $V = 9$ m/sec, Equation 16 yields $f = 9/3.2 = 2.8$ Hz. The second peak in the curves is expected to occur when $\delta = 2$, i.e., $\Delta = 2V/f = 6.4$ m. This also conforms with Figure 11a.

The spacings given by Equation 13 and shown by the vertical lines in Figures 11a and b would be reasonable choices for the array design spacings. The vertical line corresponding to $n = 2$ falls slightly to the right of the first trough in the ρ versus Δ curve in Figure 11a because the natural frequency of the vehicle is 2.8 Hz, which is slightly greater than the design frequency $\bar{f} = 2.5$ Hz. Conversely, in Figure 11b, the vertical line for $n = 2$ falls to the left of the first trough, because the natural frequency of the model is 1.9 Hz.

As explained previously, arrays with three or more sensors are more robust to frequency and speed variations because they have relatively wide, flat-bottomed plateau regions (troughs) as indicated by both the experimental and theoretical curves (Figures 11a and b). As a result, the vertical lines for $n = 3$ to 6 in both graphs lie at spacings that are appropriate choices to minimize the ECOV (ρ), despite the fact that the operating frequencies are different to the design frequency $\bar{f}$. Also, a small error in spacing of the two-sensor system caused by, say, a different vehicle speed, would cause a more rapid decrease in accuracy than for the systems with three or more sensors.

A second comparison between experiment and simulation is shown in Figures 12a and b. Figure 12a shows a graph of ρ versus Δ for Axle 5, on the four-spring tandem trailer suspension of Vehicle S4, traveling at 85 km/hr. From the y-intercept, the DLC value is approximately 11.5 percent, which corresponds to the ECOV value determined previously from the histogram in Figure 10a.

The sprung mass natural frequency of the experimental vehicle can be estimated from the first peak of Figure 12a (corresponding to $\delta = 1$) using Equation 16 ($f \approx 23.6/6.0 = 3.9$ Hz). This is significantly higher than the array design frequency $\bar{f} = 2.5$ Hz, but is within the expected range of 1.5 to 4.5 Hz discussed earlier. As a consequence, the design spacing for $n = 2$, at approximately 4.7 m in Figure 12a, is far away from the optimum at approximately 3.0 m. The RMS error for $n = 2$ at the design spacing is approximately 8.8 percent.

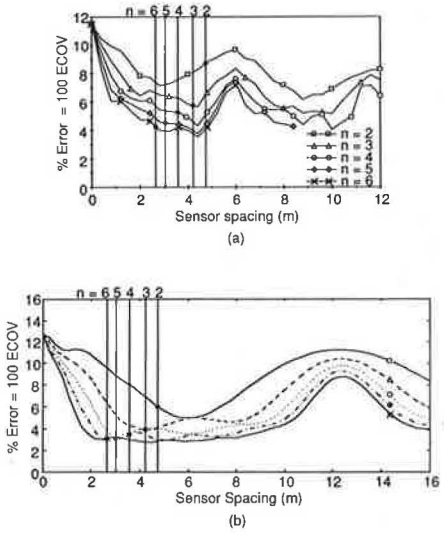

FIGURE 12 WIM array ECOV ρ versus sensor spacing Δ. Vertical lines indicate design spacings according to Equation 13, $\bar{V} = 24$ m/sec, $\bar{f} = 2.5$ Hz. (a) Experimental results for Vehicle S4, Axle 5 (on trailer), speed 85 km/hr; and (b) theoretical results for quarter-car model, speed = 85 km/hr.

The design spacing for $n = 3$ (at approximately 4.2 m) is just within the plateau region of the ρ versus Δ curve for $n = 3$. Consequently, the RMS error for $n = 3$ at the design spacing is approximately 5.7 percent, a substantial improvement over 8.8 percent, for $n = 2$. This illustrates the significant benefit, in terms of operating speed and frequency ranges, that is obtained by using a WIM array with three or more sensors. Cebon and Winkler (*7*) obtained many results similar to Figures 11a and 12a, with three-sensor WIM errors $\rho(3)$ usually in the range 3 to 7 percent for Δ_{design} chosen according to Equation 13.

Figure 12b shows theoretical predictions using the ¼-car model, with a speed of 85 km/hr. In this figure as in Figure 11b, the vertical line for $n = 2$ falls to the left of the trough in the ECOV curve for $n = 2$. This is because the natural frequency (1.9 Hz) is less than $\bar{f} = 2.5$ Hz.

Influence of Tire Tread Pattern

The contact pressure distribution under a rolling tire depends on the tread pattern. Off-road tires can have large local contact pressure variations in the vicinity of the individual tread elements. When such a tire rolls over the mat, some of the strip transducers will be loaded by high-pressure regions of the tire contact area and others will be loaded by low-pressure regions. The wheel force measurement involves integrating the output of each strip sensor (which is proportional to the local contact pressure) throughout the period of contact between tire and sensor. Thus, if some sensors experience a high contact pressure, they will register an abnormally high load. Conversely, some sensors will register an abnormally low load. This problem is dependent on the construction of the tire and the tread pattern. It is expected to occur for any type of narrow strip WIM transducers, not just capacitive strips. Thus, it can be considered to be a fundamental limit on the accuracy of strip sensors. Fortunately, the majority of highway vehicles use highway tread (rib) tires and these do not display a significant variation of local contact pressure because of the tread elements. Thus, for most vehicles, tire tread effects are not likely to cause serious errors with strip WIM sensors.

A graphic example of the tire tread effect can be seen in Figure 13 for Axle 3 of Vehicle S4, which was the only test suspension to have off-road tires. Because of the air suspension, this vehicle is expected to produce relatively small dynamic loads (*1*,*3*). However, Figure 13 shows a large value of $\rho(1)$ of approximately 16 percent at $\Delta = 0$, for a speed of 11 km/hr. This was one of the largest ECOV values measured in all of the tests. The $\rho(1)$ value for Axle 3 of Vehicle S4 was found to remain approximately constant with speed, indicating that it was not influenced by the dynamics of the vehicle. For every other suspension, there was a significant increase in $\rho(1)$ with speed.

The first peak in Figure 13 occurs at $\Delta_1 = 2.0$ m. If this peak were caused by dynamic loads, it would shift with speed. For example, if the speed increased from 11 to 85 km/hr, Δ_1 would be expected to increase to $\Delta_1 = 2.0 \times 85/11 =$

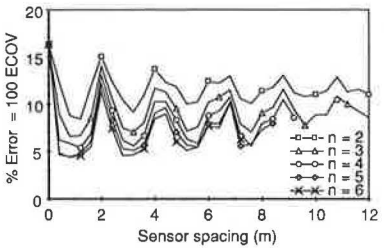

FIGURE 13 Measured WIM array ECOV ρ versus sensor spacing Δ for Vehicle S4, Axle 3 (off-road tires), speed = 11 km/hr.

15.5 m. This was not found to occur in the experimental result (7). In fact, the position of the first peak was found to stay relatively constant for speeds up to 51 km/hr and then decrease slightly with higher speeds, to $\Delta_1 = 1.8$ m at 85 km/hr.

The explanation for this behavior is related to the tire tread pattern and is described in detail by Cebon and Winkler (7). It transpires that five sensor spaces (2 m) correspond to a prime number of tire tread elements and hence the maximum contact pressure can only coincide with the location of every fifth sensor. This is an example of undersampling or aliasing. The sensor array cannot distinguish between tire contact pressure variation with wavelength equal to the tire tread interval, and a force component with wavelength 2.0 m. This result is dependent only on the tread pattern and so the aliased wavelength of 2.0 m is largely independent of speed. For high vehicle speeds, the driving torque and hence longitudinal creep or slip of the driven wheels becomes significant. This causes an effective reduction in the wavelength of the contact pressure distribution along the mat and a decrease in the aliased wavelength from 2.0 to 1.8 m.

CONCLUSIONS

1. A simple equation defining a good design spacing for the sensors in a multiple-sensor WIM system was derived from theoretical considerations and verified by experiments with a load measuring mat.

2. Arrays with three or more evenly spaced sensors will be more robust to speed and frequency variations than two-sensor systems.

3. A good design choice is to use three-sensor arrays that are likely to give RMS errors of $\frac{1}{3}$ to $\frac{1}{2}$ of the errors for single-sensor systems. In the near future, it should be possible to routinely estimate the static axle loads of vehicles traveling at highway speeds with RMS errors of approximately 5 to 8 percent (compared with 12 to 29 percent for existing systems).

4. The response of the capacitive strip sensors in the load measuring mat was found to be independent of (a) vehicle speed in the range 8 to 80 km/hr, (b) mat surface temperature in the range 15°C to 40°C, and (c) long-term drift.

5. The average sensor baseline error caused by noise was found to be less than 4 percent RMS.

6. Approximately 2.5 percent of all data was lost out of 460 test runs over the 96 sensors. Almost half of the lost data (1 percent) was caused by a single sensor that failed.

7. The strip sensors were found to be inaccurate for tires with an off-road tread pattern. This effect is a fundamental limitation of strip WIM sensor technology and is expected for any type of strip transducer.

8. No evidence was found of fore-aft static load transfer in the test vehicles because of speed.

ACKNOWLEDGMENTS

The work described in this paper was performed as part of SHRP/IDEA Project 15 and was funded jointly by The Strategic Highway Research Program (SHRP), Golden River (U.K.) Ltd., Michigan DOT, The Great Lakes Center for Truck Transportation Research (University of Michigan Transportation Research Institute), and Navistar Technical Center and Cambridge University, England. The authors would like to thank Michael Dalgleish and David Fine of Golden River Ltd., David Cole of Cambridge University, David Harrold of Navistar, and John Koch, Mike Campbell and Tom Gillespie of UMTRI.

REFERENCES

1. P. F. Sweatman. *A Study of Dynamic Wheel Forces in Axle Group Suspensions of Heavy Vehicles*. Australian Road Research Board Special Report SR27, 1983, 56 pp.
2. R. D. Ervin, R. L. Nisonger, M. Sayers, T. D. Gillespie, and P. S. Fancher. *Influence of Truck Size and Weight Variables on the Stability and Control Properties of Heavy Trucks*. University of Michigan Report UMTRI-83-10/2, Ann Arbor, April 1983.
3. C. G. B. Mitchell and L. Gyenes. *Dynamic Pavement Loads Measured for a Variety of Truck Suspensions. Proc., 2nd International Conference on Heavy Vehicle Weights and Dimensions*, Kelowna, British Columbia, 1989.
4. J. H. F. Woodrooffe, P. A. LeBlanc, and K. R. LePiane. *Effects of Suspension Variations on the Dynamic Wheel Loads of a Heavy Articulated Highway Vehicle. Vehicle Weights and Dimensions Study*, Vol. 11, Canroad Transportation Research Corporation, Ottawa, Canada, 1986.
5. M. H. Glover and W. H. Newton. *Evaluation of a Multiple-Sensor Weigh-in-Motion System*. Working Paper WP VED/90/69, Transport and Road Research Laboratory, Crowthorne, Berkshire, United Kingdom, 1989.
6. M. H. Glover. *Weighing Axles in Motion with a Multiple Sensor System*. Working Paper WP VED/88/50, Transport and Road Research Laboratory, Crowthorne, Berkshire, United Kingdom, 1988.
7. D. Cebon and C. B. Winkler. *A Study of Road Damage Due to Dynamic Wheel Loads Using a Load Measuring Mat*, Volume 1. SHRP/IDEA Project 15, UMTRI-90-13, 1990.
8. D. E. Newland. *Random Vibration and Spectral Analysis*, 2nd ed., Longman, N.Y., 1987.
9. J. D. Robson. *Road Surface Description and Vehicle Response. International Journal of Vehicle Design*, Vol. 1, No. 1, 1979.
10. D. J. Cole and D. Cebon. Simulation and Measurement of Dynamic Tyre Forces. *Proc., 2nd International Conference on Heavy Vehicle Weights and Dimensions*, Kelowna, British Columbia, 1989.
11. J. R. Morris. *Effects of Heavy Vehicle Characteristics on Pavement Response—Phase 1*. Prepared for NCHRP Project 1-25, TRB, National Research Council, Washington, D.C., Dec. 1987.
12. *Proposals for Generalised Road Inputs to Vehicles*. ISO/TC/108/WG9, Draft 3e, 1972.
13. D. J. Cole and D. Cebon. *A Capacitative Strip Sensor for Measuring Dynamic Tyre Forces. Proc., 2nd International Conference on Road Traffic Monitoring*. Institution of Electrical Engineers, London, Feb. 1989.

Publication of this paper sponsored by Committee on Vehicle Counting, Classification, and Weigh-in-Motion Systems.